Trigonal polymorph of Li_2MnO_3

B. Xia,[1] J. Cheng,[2] M. Arengo,[1] N. Rajput,[1] Y. Janssen,[1] J. R. Neilson,[3] K. A. Persson,[2,4] and J. W. Simonson[1,*]

[1]*Department of Physics, Farmingdale State College, Farmingdale, New York 11735, USA*

[2]*Energy Technologies Area, Lawrence Berkeley National Laboratory, Berkeley, California 94720, USA*

[3]*Department of Chemistry, Colorado State University, Fort Collins, Colorado 80523, USA*

[4]*Department of Materials Science and Engineering, University of California, Berkeley, California 94720, USA*

(Received 14 June 2020; accepted 28 July 2020; published 10 August 2020)

We report the discovery of a trigonal polymorph of the prospective Li-ion battery material Li_2MnO_3 and its synthesis in bulk, single-crystal form. Crystal growth of trigonal Li_2MnO_3 is strongly dependent upon the quality of a polycrystalline $LiMnO_2$ precursor consumed in the synthesis process. The crystal structure of the trigonal phase is composed of ordered honeycomb layers of LiO_6 and MnO_6 octahedra segregated by layers of LiO_6 octahedra and represents an ordered stacking variant of the known monoclinic polymorph. Diffuse reflectance spectroscopy reveals a direct optical gap of 2.47 ± 0.11 eV and a series of charge excitations that are well explained by the expected Mn^{4+} $3d^3$ valence. Density functional theory calculations are in excellent agreement with the spectroscopic measurements and find a near degeneracy in the formation energies of the two polymorphs. Our results suggest that the trigonal structure resolves the compositional and structural disorder often manifested in the monoclinic phase.

DOI: 10.1103/PhysRevMaterials.4.085401

I. INTRODUCTION

One of the central challenges in experimental materials synthesis lies in selecting among two or more compounds when the differences between their energies of formation are much smaller than the energy scale kT required to initiate phase formation [1–3]. This issue is particularly challenging when these compounds have the same composition, making understanding the local energy landscape critical to controlling the crystallization pathways and driving the reaction to the desired product [4]. Nonetheless, this level of control has been experimentally realized in several systems. In the case of TiO_2, for instance, selective synthesis of various metastable polymorphs has been achieved through direct observation of crystallite nucleation and *in situ* control of Ti coordination environments from amorphous TiO_2 precursors [5,6]. Similarly, the selection of crystallization pathways to form desired $CuSe_2$ polymorphs was found to be primarily controlled by exposure to air and humidity [7], while MnO_2 polymorphs can be selected by varying K^+ concentrations in hydrothermal reactions [8].

In the overwhelming majority of multinary oxide systems, however, the temperatures required for synthesis exceed 1000 K, often precluding such a precise level of control over synthetic pathways. A potential solution to this challenge lies in identifying reactive intermediaries that modify the energy landscape towards controlled stabilization of the target compound, a technique that recently has been comprehensively demonstrated in the synthesis of yttrium manganese oxides [9,10], Mn nitrides [11], pyrite FeS_2 [12], and cuprate superconductors [13]. Along these lines, we recently showed the *in situ* formation of an intermediate ternary oxide to be critical in triggering the growth of $Li_2Mn_2(MoO_4)_3$ single crystals [14]. Furthermore, the very technique of growing single crystals from molten solutions provides an additional set of levers for accessing the energy landscape, through which synthesis temperatures, redox equilibria, coordination environments, and even the stabilization of desirable metal complexes can be controlled [1,15,16].

The structure of the room temperature monoclinic polymorph of Li_2MnO_3 has been known for several decades [17] and consists of honeycombed layers of Li- and Mn-centered octahedra separated by layers of wholly Li-centered octahedra. Static and fluctuating moments confirm the expected Mn^{4+} valence configuration [18,19]. Li and Mn occupancy mixing within the Li/Mn layer is common [20], but in the ostensibly unmixed case, adjacent Li/Mn honeycomb layers are stacked neatly on top of each other along the monoclinic c axis [21]. Electron diffraction and high-resolution transmission electron microscopy (HRTEM) measurements shed light on a complicated defect physics, revealing intrinsic stacking faults among the Li/Mn layers [22]. The frequency of these stacking faults is closely tied to the method of synthesis across both sol-gel and solid-state reaction techniques, and significant gaps remain in our understanding of the complete relationships among synthesis, structure, and cathode performance [23].

Density functional theory (DFT) calculations provide insight into this complicated interplay, finding that nucleation sites for impurity phases can be adjusted or eliminated by tuning synthesis conditions [24] and that both the Li and Mn sites are energetically favorable for various chemical dopants [25,26]. In near-stoichiometric monoclinic Li_2MnO_3, Mn migration and O outgassing are both found to be

*jack.simonson@farmingdale.edu

thermodynamically unfavorable, while both the mixed Li/Mn and unmixed Li structural layers permit facile delithiation [27]. Taken together with experimental reports, these computational results suggest that monoclinic Li_2MnO_3 is situated at a point in the energy landscape at which many nearly degenerate minima closely coexist and can be accessed by minute changes in synthesis conditions.

In this light, it is not altogether surprising that a trigonal polymorph of Li_2MnO_3 was predicted in the last few years on the basis of atom model simulations of selected-area electron diffraction (SAED) images, yielding a hitherto unobserved phase with the noncentrosymmetric space group $P3_112$ and consisting of three stacking configurations rotated by 120° with respect to one another [28]. Rigorous examination of HRTEM measurements, however, showed the images lacked conclusive evidence of the proposed phase.

We report here the experimental realization in the bulk, single-crystal form of a polymorph of Li_2MnO_3 with the trigonal space group $P3_112$. We present the crystal structure of this so-called trigonal Li_2MnO_3, as well as our procedure to grow high-quality single crystals of this material from molten halide and oxide polycrystalline precursors. UV/visible (Vis) optical spectroscopy measurements carried out on these crystals show an insulating ground state with an $E_g = 2.47 \pm 0.11$ eV charge gap and absorption edges consistent with octahedrally coordinated $3d^3$ Mn. DFT electronic structure calculations closely reproduce these results and find that trigonal Li_2MnO_3 is nearly degenerate in formation energy with its previously known monoclinic polymorph.

II. METHODS

We grew high-quality single crystals of trigonal Li_2MnO_3 from a molten oxyhalide solution by loading an intimate mixture of powders with a total mass of 0.98 g and with atomic ratio $(LiMnO_2)_{0.06}(Li_2O)_{0.11}(LiCl)_{0.83}$ into a 99.9% fine Ag silver crucible that had been flame sealed at one end. We selected the Li_2O/LiCl-based solution because the solubility of Li_2O in LiCl as a function of T is so precisely known, and the sole precipitant from a pure, molten Li_2O/LiCl solution is Li_2O [29]. Because we handled the powders in air and LiCl is known to be strongly hygroscopic, we evacuated the filled crucible with a roughing pump to 30 mTorr for 30 min. We then promptly crimped close the open end of the Ag crucible, folded over the crimped portion, and recrimped and refolded two more times. Immediately after thus sealing the crucible, we placed it in a furnace that had been preheated to 473 K. The furnace temperature was then uniformly ramped to 1173 K over a period of 120 min, held at this temperature for 120 min, and gradually cooled to 873 K over a period of 3600 min, whereupon we removed the sealed Ag crucible from the furnace.

Upon extraction, we observed a slight bulging of the crucible itself—which we presume may be due to the expansion of remnant water vapor—as well as the formation of Ag dendrites on the crucible exterior. Given that Ag is soluble in HCl, we hypothesize that HCl was formed *in situ* by $LiCl + H_2O \rightarrow LiOH + HCl$. This reaction is unlikely to be enthalpy driven at room temperature but may occur due to a steam-driven process, and previous computational and theoretical

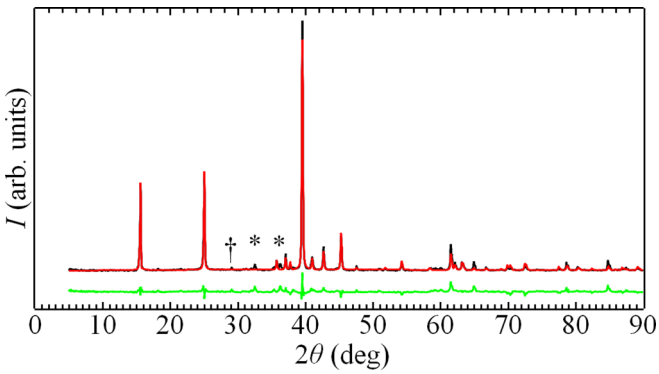

FIG. 1. The powder x-ray diffraction pattern (black) and Rietveld refinement (red) of a polycrystalline $LiMnO_2$ precursor. The difference between the observed and calculated patterns is shown below in green. Small peaks that are not indexed by the *Pmmn* $LiMnO_2$ parameters correspond to remnant Mn_2O_3 and Li_2CO_3 and are denoted by * and †, respectively.

work has found the potential for ion exchange in saturated LiCl-LiOH-H_2O and LiCl-HCl-H_2O ternary systems [30] as well as direct hydrolysis of LiCl → LiOOH near 1073 K [31]. Accordingly, we conclude that trace H_2O may play a role in tuning the Li-rich solution central to our synthesis process.

Upon opening the crucible at ambient temperature, we washed away the regulus with deionized water. The resulting hundreds of crystals took the form of transparent red platelets of hexagonal habit as large as 100 μm across, an example of which we show in Fig. 2(a) below. The phase purity of

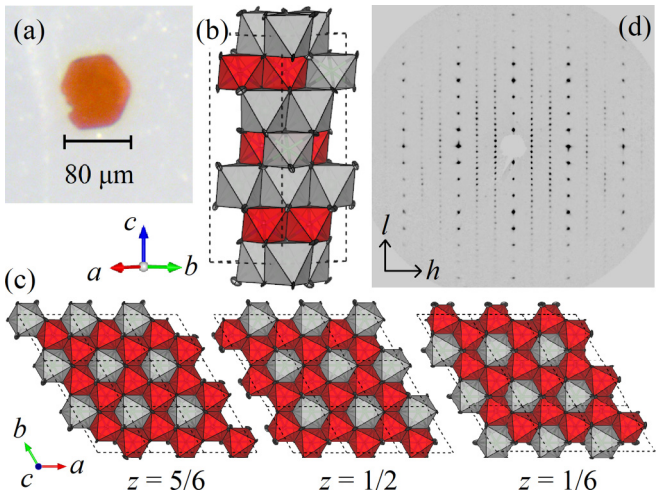

FIG. 2. (a) An optical microscope image of a typical single crystal of trigonal Li_2MnO_3. (b) The unit cell of trigonal Li_2MnO_3. Mn and Mn-centered octahedra are colored red, Li and Li-centered octahedra are colored light gray, and O is colored dark gray. (c) A view along c of the three configurations of the Mn-containing layers, centered at $z = 5/6$, $z = 1/2$, and $z = 1/6$, as indicated. Colors are as in (b). The borders of the unit cells are marked by dashed lines. (d) The $h0\ell$ reciprocal space plane, showing no additional reflections, which would arise from an additional ordering of the stacking arrangement of the Mn-containing layers beyond that of the unit cell.

polycrystalline precursors to the crystal growth routine was confirmed by powder x-ray diffraction with a Rigaku MiniFlex and Cu $K\alpha$ radiation. We determined the crystal structure of trigonal Li_2MnO_3 using an Oxford Gemini single-crystal diffractometer with Mo $K\alpha$ radiation, obtaining some 49,756 reflections with 99.8% completeness over the full reciprocal space sphere out to a resolution of 0.55 Å. Reflections were analytically corrected for absorption by face indexing of the crystal [32]. We solved the structure by employing a charge-flipping algorithm [33–35]. We collected UV-Vis diffuse reflectance spectra with photon wavelengths from $\lambda =$ 900 to 250 nm in a Cintra 40 double-beam spectrometer with an integrating sphere and using $BaSO_4$ as a reference. The resolution in λ was 1.0 nm.

We carried out DFT electronic structure calculations using the Vienna *Ab initio* Simulation Package (VASP) [36,37], with projector augmented-wave potentials [38]. The spin-polarized generalized gradient approximation (GGA) parametrized by the Perdew-Burke-Ernzerhof functional [39] employing the on-site Coulomb interaction approach (GGA + U) was used for the exchange-correlation functional with $U = 3.9$ eV for Mn 3d orbitals [40]. A ferromagnetic configuration was employed for both monoclinic and trigonal Li_2MnO_3. We also considered an antiferromagnetic configuration along [100] for trigonal Li_2MnO_3 and found the total energy is only 2 meV/atom higher, which indicates that the effect of spin ordering on the total energy is very small [41,42]. The cutoff energy for the plane wave expansion was set to 520 eV, and all structures were optimized using an electronic self-consistency convergence criterion of less than 2×10^{-5} eV. The k-point grids for Brillouin zone sampling were set to $6 \times 6 \times 6$ for monoclinic Li_2MnO_3 and $6 \times 6 \times 2$ for trigonal Li_2MnO_3.

III. RESULTS AND DISCUSSION

Solution growth of single crystals of trigonal Li_2MnO_3 is highly dependent on the polycrystalline precursors dissolved within the flux and particularly on $LiMnO_2$, which acts as the sole source of Mn. Because the reproducibility of the crystal growth procedure that we describe above hinges so sensitively on this precursor, we will devote some discussion here to our method for its synthesis. We first formed Mn_2O_3 by calcining commercially available 99% pure MnO in air at $T = 973$ K for 24 h. We then synthesized $LiMnO_2$ from the solid-state reaction of a 6.35-mm-diameter pressed pellet with a mass of 1.00 g of this Mn_2O_3 intimately mixed with commercially available 99% Li_2CO_3. The pellet was placed in an Al_2O_3 crucible and sealed in an evacuated quartz ampoule with an outer diameter of 28 mm and length of 10 cm. The large volume of the ampoule relative to that of the pellet is required to accommodate outgassing of CO_2 from Li_2CO_3 during heat treatment. The sealed ampoule was then heated to 1023 K in 120 min and held at this temperature for 960 min, whereupon the furnace power was abruptly cut, and the sample was removed after the furnace had cooled to 800 K. We caution that appropriate care must be taken in removing the ampoule from the furnace as it remains pressurized at this temperature. The resulting powder was dark reddish brown.

We show in Fig. 1 the powder x-ray diffraction pattern of a polycrystalline $LiMnO_2$ powder obtained from this process. The pattern corresponds to the room temperature orthorhombic polymorph with space group *Pmmn* (No. 59). Small unindexed peaks at diffraction angle $2\theta =$ 29.12°, 32.54°, and 36.29° reveal remnant unreacted Mn_2O_3 and Li_2CO_3, as indicated in Fig. 1, but do not inhibit crystal growth in these $O(1\%)$ concentrations. On the other hand, $LiMnO_2$ precursor powders with significantly larger concentrations of unreacted Mn_2O_3 and Li_2CO_3, as well as precursors of lower crystallinity with larger FWHMs were unable to produce single crystals of the desired trigonal Li_2MnO_3 phase and instead resulted in polycrystalline products or dark, lustrous single crystals of cubic $LiMn_2O_4$.

We observed that following precisely the crystal growth procedure as discussed above and in Sec. II is critical to obtaining the trigonal Li_2MnO_3 single crystals. Our preliminary experiments using LiOH as a Li source resulted in crystals of $LiMn_2O_4$, while introducing LiI proved to be incompatible with Ag tubing. Attempting to reduce the maximum soak temperature to 923 K resulted instead in poor-quality crystals of $LiMnO_2$ as well as polycrystalline material. Increasing the crystal growth time resulted in corrosion of the Ag tube and formation of a brick-red polycrystalline material. Additionally, growths in which we did not observe the formation of Ag dendrites did not result in crystals of the desired phase, implying that H_2O plays an important role in this synthesis. Altogether, these preliminary experiments underscore the narrow range of synthesis conditions that are capable of yielding the trigonal Li_2MnO_3 phase.

Figure 2 presents a visualization of the crystal structure of trigonal Li_2MnO_3, which, like the known monoclinic polymorph, consists of two layers with distinct compositions stacked along the crystallographic c direction. This longest lattice parameter c is oriented normal to the hexagonal face of the crystal shown in Fig. 2(a), as is typical. One of the two layers is entirely composed of edge-sharing LiO_6 octahedra, and the other is characterized by a honeycomb structure in which each LiO_6 octahedron edge shares with six adjacent MnO_6 octahedra with an overall Li:Mn ratio of 1:2 within the layer. Individually, each of these components is identical to the equivalent layer in the ostensibly unmixed variety of monoclinic Li_2MnO_3.

On the other hand, as seen from the unit cell in Fig. 2(b), the Li-/Mn-containing layers are stacked with three distinct Li/Mn configurations centered at fractional c axis coordinate $z = 1/6$, $1/2$, and $5/6$, effectively breaking the unit cell into thirds. Figure 2(c) depicts a top-down view of three adjacent Li/Mn layers across a plaquette of $3 \times 3 \times 1/6$ unit cells within the *ab* plane, providing insight into the details of this ordered stacking arrangement. In each layer, the honeycomb pattern itself is obvious from the figure, but this configuration is translated by $-1/3$ of the unit cell along a from the $z = 5/6$ to $z = 1/2$ layers and again by $+1/3$ along a and $+1/3$ along b from the $z = 1/2$ to $z = 1/6$ layers. These translations are equivalent to 120° rotations of these layers, just as predicted by previous atom model simulations [28]. The strongly scattering Mn positions within these three distinct layers are incompatible with inversion symmetry, and attempts to refine our data with the most closely related centrosymmetric space group P-3m1 (No. 162) do not converge with physically reasonable solutions. If we force the structure into

TABLE I. The structural parameters of trigonal Li_2MnO_3 measured at $T = 294$ K by single–crystal x-ray diffraction. The space group is $P3_112$ (No. 151), and the lattice parameters are $a = b = 4.9243(2)$ Å, $c = 14.2141(5)$ Å, $\alpha = \beta = 90°$, $\gamma = 120°$, $V = 298.50(2)$ Å^3. Refinement was carried out on the square of the observed structure factors F^2_{obs} with the final values for the goodness of fit parameters, residuals, and weighted residuals for observed and all reflections obtained as $S_{obs} = 1.97$, $S_{all} = 1.79$, $R_{obs} = 0.0340$, $wR^2_{obs} = 0.0925$, $R_{all} = 0.0476$, and $wR^2_{all} = 0.0975$.

Atom	Site	x	y	z	U_{eq} (Å^2)
Mn1	3*b*	0.4447(3)	0.5553(3)	5/6	0.0039(4)
Mn2	3*b*	0.77659(16)	0.22341(16)	5/6	0.0040(4)
O1	6*c*	0.1109(12)	0.2491(7)	0.90916(10)	0.0037(7)
O2	6*c*	0.1069(14)	0.5304(8)	0.7590(4)	0.0062(9)
O3	6*c*	0.7541(11)	0.5347(8)	0.9078(4)	0.0063(10)
Li1	3*b*	1.1067(17)	0.8933(17)	5/6	0.0003(9)
Li2	3*a*	0.422(3)	0.2112(14)	1	0.012(3)
Li3	3*a*	0.094(4)	0.5468(19)	1	0.010(3)
Li4	3*a*	0.1101(12)	0.220(2)	2/3	0.0127(10)

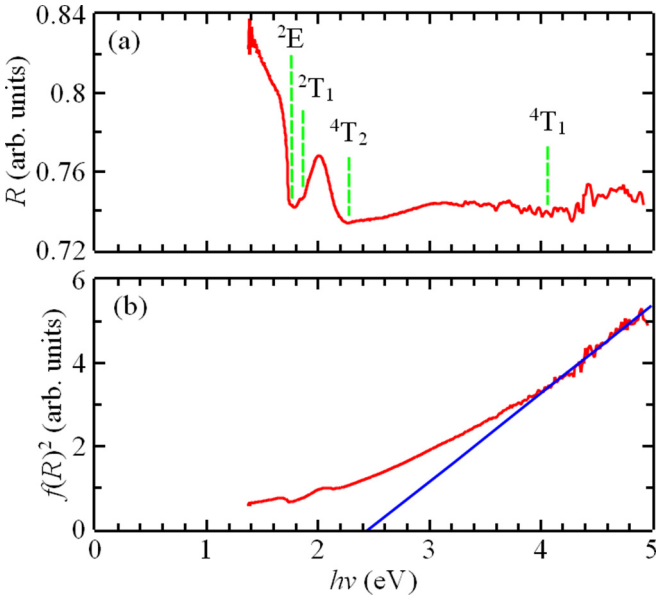

FIG. 3. (a) The UV/Vis diffuse reflectance R vs the energy $h\nu$ spectrum of trigonal Li_2MnO_3 (red). The green dashed vertical lines mark the likely locations of transitions of octahedrally coordinated Mn^{4+} $3d^3$ from its $^4A_2$ ground state to the indicated excited states. (b) The Kubelka-Munk plot of the reflectance data (red). The solid blue line is a linear regression to $f(R)^2$ for $h\nu > 4.0$ eV and corresponds to the Tauc relation for direct optical gap $E_g = 2.47(11)$ eV.

P-3*m*1, these Mn positions are accordingly doubled within the threefold rotational plane to accommodate the inversion operator, leading to irregular hexagons of Mn with unphysical interatomic distances of 1.03 and 0.80 Å between nearest neighbors. We conclude that the data can be explained only by the noncentrosymmetric space group, as was predicted previously [28], or else by an extremely disordered structure that is incompatible with subsequent measurements and calculations.

Given the preponderance of stacking faults and variations in monoclinic Li_2MnO_3, we carefully searched for evidence of the same in our trigonal single crystals. Accordingly, Fig. 2(d) shows an unwarped image of the $h0\ell$ reciprocal space plane as integrated from diffraction images. We collected data out to a resolution of $d = 0.55$ Å, corresponding to ± 7 reciprocal lattice units (r.l.u.) in the $a^\star$ direction and ± 25 r.l.u. in $c^\star$. Reflections are round and discrete even at the limits of our resolution, indicating a high degree of crystal uniformity over many adjacent unit cells. The average crystal mosaicities are small, coming to 1.21°, 1.08°, and 1.25° along each reciprocal space direction as defined locally about each reflection. We do not observe any systematic pattern of reflections that cannot be indexed by the lattice parameters, which might indicate a stacking-related superstructure or a structural modulation. Nor do we observe any diffuse scattering such as what might accompany a systematic abundance of more or less random stacking faults. Barring more direct evidence like what might be obtained from HRTEM images, we infer that if stacking faults are present in our crystals of trigonal Li_2MnO_3, they occur with substantially less regularity than the 40%–60% faulting probabilities observed in the monoclinic polymorph [23].

Table I shows the crystallographic details of our solution, including atomic positions and displacement parameters corresponding to the structure depicted in Fig. 2. Here we see that the Li/Mn layers are composed of two crystallographically inequivalent Mn sites and a single Li site, each located at a 3*b* Wyckoff position. Similarly, the Li layer consists of three additional crystallographically inequivalent Li sites, each at a 3*a* position. Bond valence sum calculations give predicted Mn valences of 3.90(2) and 3.93(2) for the Mn1 and Mn2 sites, respectively, consistent with the Mn^{4+} $3d^3$ atomic configuration expected from elementary valence counting and from the observed similarities in local structure shared with the monoclinic polymorph.

Although the atomic displacement parameters U_{eq} given in Table I are nearly all realistic and mutually consistent, one value in the tabulated data requires additional inspection: we note that the U_{eq} corresponding to the Li1 site—the single Li site located within the Li/Mn layer—is unphysically small, suggesting that the atom located at this position remains unrealistically static in response to thermal vibrations. Such an unphysically small thermal displacement parameter may indicate that more charge is located at this position than our structural model permits. Accordingly, if we unfix the Li occupancy at this position in our refinement so that this quantity is allowed vary freely in response to this excess observed charge, it will refine to some 19% additional Li at the position, which is certainly impossible. The corresponding additional free refinement parameter leads to a very modest ∼1% relative improvement in refinement statistics. This apparent 19% excess of Li likely corresponds instead to an ∼2% Mn occupancy on the Li1 site. Given this small percentage, we were not able to refine any purported mixed-site occupancy with any degree of certainty, but it is possible that a slight nonstoichiometry just at the verge of our resolution may be related to the stabilization of the trigonal phase, and we speculate that its true composition may be approximately $Li_{1.995}Mn_{1.005}O_3$.

Figure 3 shows strong agreement with the expected octahedrally coordinated Mn^{4+} $3d^3$ state inferred from our crystallographic analysis and furthermore reveals that trigonal Li_2MnO_3 is a narrow-gap insulator, much like its monoclinic polymorph. In Fig. 3(a), we plot the background-subtracted diffuse reflectance R spectrum of a collection of single crystals oriented so that light is incident along their crystallographic c axes. R increases steeply at the low-energy $h\nu$ limit of our measurement, indicating that the crystals are nearly transparent to infrared radiation, as expected of an insulator. R falls sharply as $h\nu$ increases through the near infrared, reaching a minimum near $h\nu \sim 1.75$ eV, an energy consistent with transitions from the Mn ground state to the first excited doublet state $^4A_{2g}(^4F) \rightarrow {}^2E_g(^2G)$ in octahedrally coordinated Mn^{4+} oxides [43,44]. This transition corresponds to no change in orbital character (i.e., $t_2^3 \rightarrow t_2^3$) and is spin forbidden but nevertheless occurs due to spin-orbit coupling to spin-allowed states of similar $h\nu$. A shoulder adjacent to this minimum at $h\nu \sim 1.86$ eV then corresponds to a similarly spin forbidden transition from the ground state to the first excited quartet state $^4A_{2g}(^4F) \rightarrow {}^2T_{1g}(^2G)$. The local maximum just above this transition at $h\nu \sim 2.0$ eV is in excellent agreement with the observed red color of the crystals, while above this maximum, we observe a second local minimum at $h\nu \sim 2.25$ eV that likely is associated with a spin-allowed transition to the second excited quartet state $^4A_{2g}(^4F) \rightarrow {}^4T_{2g}(^4F)$ associated with the promotion of an electron from the O_h-stabilized t_2 states to an e state (i.e., $t_2^3 \rightarrow t_2^2e$). Finally, a second spin-allowed transition associated with $^4A_{2g}(^4F) \rightarrow {}^4T_{1g}(^4F)$ and $t_2^3 \rightarrow t_2^2e$ is expected for higher $h\nu$ $3d^3$ transitions [43–45]. The location of this transition is obscured by noise in our $BaSO_4$ reference subtraction but may be just resolvable near $h\nu \sim 4$ eV. As a whole, the appearance in our spectrum of these three to four expected transitions purports that the Mn species is tetravalent—consistent with the results of our crystallographic analysis—and moreover is subject to spin-orbit interactions.

Figure 3(b) plots the square of the Kubelka-Munk function $f(R)^2$, the extrapolated $h\nu$ intercept of which permits estimation of the optical charge gap. For $h\nu > E_g$, the Tauc relation $\alpha h\nu = C(h\nu - E_g)^\beta$ approaches linearity, where α signifies the absorption coefficient, C is a geometry-dependent parameter, and the exponent β is related to the nature of the gap. Our linear regression for $h\nu > 4.0$ eV is clearly superior when $\beta = 1/2$, suggesting a direct gap, and the intercept gives a magnitude of $E_g = 2.47(11)$ eV. The experimental optical gap of monoclinic Li_2MnO_3, on the other hand, is reported to be substantially narrower with $E_g = 2.05$–2.1 eV [46], which is curious given the profound local structural similarities between the two polymorphs. Consequently, we speculate that the relative lack of site mixing and stacking faults in trigonal Li_2MnO_3, as suggested by our crystallographic measurements, may be the primary cause of the relatively wider gap in this system.

Motivated by the discrepancy in the experimental charge gaps between the two polymorphs, we further investigated the electronic structure of trigonal Li_2MnO_3 by carrying out DFT calculations, which reproduce the direct experimental gap. As we show in Fig. 4(a), the band structure of trigonal Li_2MnO_3 features a direct band gap of 2.01 eV and a nearly identical indirect band gap of 1.99 eV with the conduction band minimum (CBM) located at the K point of the first Brillouin zone and the valance band maximum (VBM) situated at the H point. It is well established that DFT systematically underpredicts band gaps, mainly due to spurious electron-electron self-interaction, which explains the modest discrepancy we find between observed and computed gaps.

Figure 4(b) shows the layer-resolved density of states (DOS) for the three distinct Li/Mn layers centered at $z = 5/6$, $z = 1/2$, and $z = 1/6$, as depicted in Fig. 2(c). Our calculations find nearly identical densities of states for each Li/Mn layer in trigonal Li_2MnO_3, revealing identical Li and Mn coordination states in each of these layer. The calculations imply that any empirically arising discrepancies between the two polymorphs, such as the extent of the gap, are primarily caused by the previously reported preference for chemical and/or structural disorder in the monoclinic phase.

We plot the spin-polarized total and partial DOSs in Fig. 4(c) to illustrate the contributions of atomic orbitals in the states near the VBM and CBM of trigonal Li_2MnO_3, which are again consistent with the results of spectroscopic measurements. We find that the DOS near the top of the valence band—within ∼1 eV of the VBM—is predominantly composed of nearly dispersionless O $2p$ states, while the lowest ∼1 eV of the conduction band above the CBM consists of strongly hybridized Mn $3d$ and O $2p$ states. Subsequent states deeper in the conduction band are primarily Mn $3d$ in character. Thus, in addition to the excellent correspondence between the calculated gap and experiment, the resulting picture of strongly hybridized Mn-O bands in the vicinity of the gap is consistent with our identification of Mn^{4+} transitions in spectroscopic measurements in a crystal field arising from O-capped octahedra.

For purposes of comparison, we calculated the electronic structure of the known monoclinic polymorph of Li_2MnO_3 following the same procedure and with the same $U = 3.9$ eV. Although chemical and structural disorders are typically observed in this polymorph, we performed the calculation in their absence. The resulting calculated direct and indirect band gaps of monoclinic Li_2MnO_3 are 1.94 and 2.16 eV, respectively, in agreement with previous theoretical results [41] and nearly the same as our calculated gap of trigonal Li_2MnO_3. As expected, both structures also contain the same atomic orbital contributions at VBM and CBM. These results underscore the similarity of both structures, at least in the disorder-free limit. We are left to conclude that if the electronic structures of the two polymorphs are nearly identical when mixed site occupancies and stacking faults are absent from the calculations, any experimentally observed narrowing of the gap in the monoclinic polymorph is likely to stem from these and other forms of disorder.

We furthermore evaluated the phase stability of trigonal Li_2MnO_3 by building the energy convex hull in the Li-Mn-O chemical space. We find that the energy above this hull is only 0.9 meV/atom; that is, the formation energy of the trigonal polymorph of Li_2MnO_3 is just 0.9 meV/atom higher than that of its monoclinic counterpart. Such a small energy difference

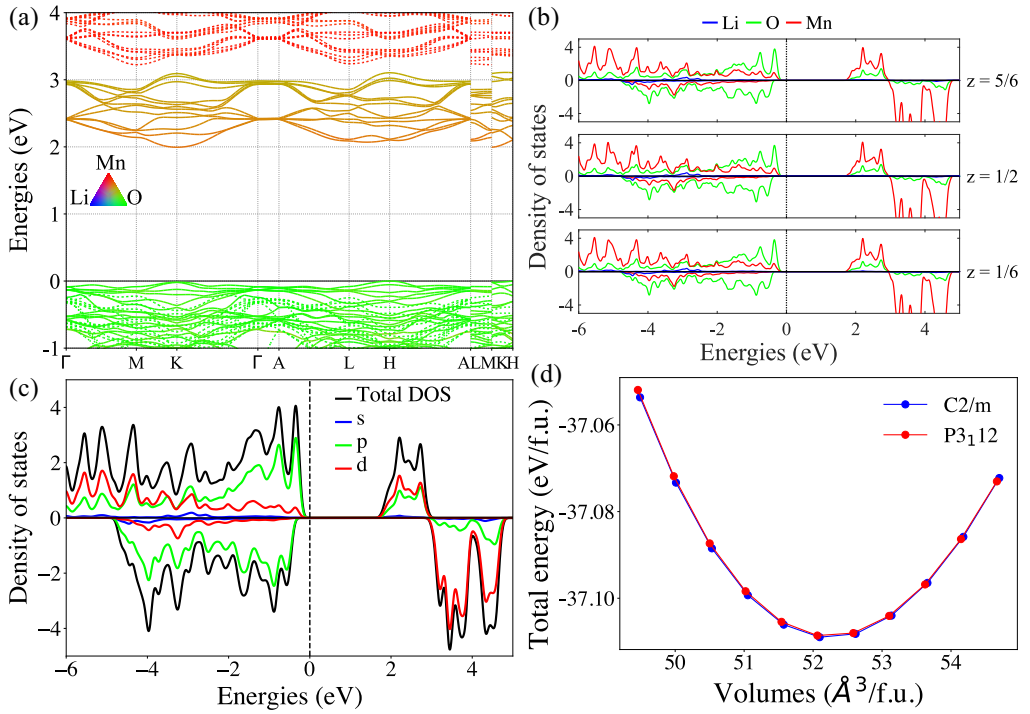

FIG. 4. (a) The calculated band structure of trigonal Li_2MnO_3 with GGA + U (U = 3.9 eV) as obtained from DFT calculations. The color table inset shows the atomic contributions to each band, with bands of primarily Li character shown in blue, Mn character in red, and O character in green, as indicated. Energies are plotted relative to the valance-band maximum. The set of high-symmetry points was generated by PYMATGEN [47]. (b) Layer-resolved density of states for the three distinct Li/Mn configurations centered at fractional c-axis coordinate $z = 1/6$, $1/2$, and $5/6$ in trigonal Li_2MnO_3. The vertical dashed line represents the Fermi level. Li-derived states are shown in blue, O-derived states are in green, and Mn-derived states are in red, as indicated. (c) The total (black) and partial densities of states per formula unit for trigonal Li_2MnO_3, with s-derived states in blue, p-derived states in green, and d-derived states in red, as indicated. (d) Calculated total energy as a function of unit cell volume for monoclinic ($C2/m$; blue) and trigonal ($P3_112$; red) Li_2MnO_3 structures.

falls within the uncertainties and errors associated with DFT [48], which may imply that GGA + U is not accurate enough to resolve the energy difference between the two polymorphs. On the other hand, a near degeneracy of the two polymorphs is unsurprising, given that they are stacking variants—with the trigonal phase built out of two stacking configurations of the monoclinic phase—and host identical layers with apparently identical local physics. In addition, we point out that we have not observed any experimental transformation between the two polymorphs. To explore potential transformation conditions further, we calculated the total energy as a function of unit cell volume for both the trigonal and the disorder-free monoclinic phase, as we show in Fig. 4(d). Here we plot these total energies across an ∼5% relative volume expansion and contraction, such as might occur if Li_2MnO_3 were subject to wide temperature or pressure ranges of several hundred kelvins or several gigapascals, respectively [49]. The total energies of these two structures respond nearly equally to volume change, which implies that the condition for phase transformation is unlikely to be driven by pressure or thermal expansion. Therefore, it appears that the apparent preference for the monoclinic phase via most synthetic routines is primarily caused by its preference for disorder. Accordingly, we speculate that the chemistry of the crystal growth solution could be the driving factor that discriminates which phase ultimately forms.

IV. CONCLUSIONS

We have presented the crystal structure of a trigonal polymorph of Li_2MnO_3 as well as a detailed method for obtaining bulk single crystals of the same. Our results verify recent predictions arising from atom model simulations of SAED data [28] and specifically confirm the predicted space group and the presaged 120° rotational configurations adopted by three distinct Li- and Mn-containing honeycomb layers. What is more, our combined crystallographic, UV/Vis spectroscopic, and DFT analyses reveal the local Mn environment is virtually identical to that of the monoclinic polymorph, and bond valence sums and observed optical transitions together support the expected Mn^{4+} $3d^3$ ground state in trigonal Li_2MnO_3. In a word, trigonal Li_2MnO_3 appears to be a relatively disorder free analog of the monoclinic polymorph, in which energetic preferences for stacking faults and mixed occupancy in the latter are instead resolved through an ordered stacking arrangement of three distinct Li- and Mn-containing structural layers that together exhibit threefold rotational symmetry.

Given their similar local atomic environments, perhaps the most significant difference to emerge between the two polymorphs lies in the size of the optical gap, with the trigonal stacking variant apparently increasing the width of this feature. We surmise that this wider gap may result from the apparent sparsity of stacking faults and mixed site

occupancies in the trigonal polymorph. In contrast to the prevalence of these features in the monoclinic structure [22,23], our crystallographic characterization reveals an approximate upper limit of 0.5% mixing among Li and Mn sites per formula unit, and moreover, we see no coherent scattering in reciprocal space maps like what would arise from a stacking-related superstructure or modulation, nor do we observe diffuse scattering about these positions, which would stem from more or less random stacking faults. This argument is supported by DFT calculations, which find nearly the same electronic structures and gaps between the two polymorphs when such calculations are performed in the absence of such forms of disorder. Even so, we caution that a thorough inspection of disorder and stacking in trigonal Li_2MnO_3 awaits detailed HRTEM measurements that are beyond the scope of the present work.

Moving forward, a full characterization of the suitability of this material for battery technology applications must depend upon the synthesis of larger samples. Oxygen stability in monoclinic Li_2MnO_3 is a critical factor limiting its performance. Given the similarity between the two polymorphs, we expect oxygen to be stable in fully lithiated trigonal Li_2MnO_3 and thermodynamically inclined to surface oxygen release during delithiation, as has been previously clarified for the monoclinic phase [50]. We do note that it has been well established that monoclinic Li_2MnO_3 must first be "activated," a process that primes the material for electrochemical performance by initiating chemical and structural disorder [51,52]. Indeed, the presence of chemical disorder in the monoclinic polymorph—and of stacking faults in particular—appears to be integral to cathode performance [53], suggesting that the relative absence of these features in this more perfect trigonal analog may turn out to be detrimental to eventual battery applications. It remains to be seen whether trigonal Li_2MnO_3 can likewise be activated and how any thusly initiated structural disorder will evolve with repeated charging and discharging.

ACKNOWLEDGMENTS

This work was supported as part of GENESIS: A Next Generation Synthesis Center, an Energy Frontier Research Center funded by the U.S. Department of Energy, Office of Science, Basic Energy Sciences under Award No. DE-SC0019212. The Stony Brook University single-crystal diffractometer was obtained through the support of National Science Foundation Grant No. CHE-0840483.

B.X. and J.W.S. conceived of the work. The crystal growth process was designed by B.X. Synthesis of polycrystalline precursors was carried out by B.X. and M.A. with contributions from N.R., J.R.N., and J.W.S. X-ray diffraction measurements were performed by J.W.S., and the crystal structure was solved by B.X., Y.J., and J.W.S. DFT calculations and subsequent analyses were performed by J.C. and K.A.P. UV/Vis measurements and analyses were performed by B.X. and J.W.S. All authors contributed to writing the paper.

[1] D. P. Shoemaker, Y.-J. Hu, D. Y. Chung, G. J. Halder, P. J. Chupas, L. Soderholm, J. F. Mitchell, and M. G. Kanatzidis, Proc. Natl. Acad. Sci. U.S.A. **111**, 10922 (2014).

[2] C. J. Bartel, S. L. Millican, A. M. Deml, J. R. Rumptz, W. Tumas, A. W. Weimer, S. Lany, V. Stevanović, C. B. Musgrave, and A. M. Holder, Nat. Commun. **9**, 4168 (2018).

[3] K. Alberi, M. B. Nardelli, A. Zakutayev, L. Mitas, S. Curtarolo, A. Jain, M. Fornari, N. Marzari, I. Takeuchi, M. L. Green, M. Kanatzidis, M. F. Toney, S. Butenko, B. Meredig, S. Lany, U. Kattner, A. Davydov, E. S Toberer, V. Stevanovic, A. Walsh, N.-G. Park, A. Aspuru-Guzik, D. P. Tabor, J. Nelson, J. Murphy, A. Setlur, J. Gregoire, H. Li, R. Xiao, A. Ludwig, L. W. Martin, A. M. Rappe, S.-H. Wei, and J. Perkins, J. Phys. D. **52**, 013001 (2019).

[4] Z. Jiang, A. Ramanathan, and D. P. Shoemaker, J. Mater. Chem. C **5**, 5709 (2017).

[5] J. S. Mangum, L. M. Garten, D. S. Ginley, and B. P. Gorman, J. Am. Ceram. Soc. **103**, 2899 (2020).

[6] J. Buckeridge, K. T. Butler, C. R. A. Catlow, A. J. Logsdail, D. O. Scanlon, S. A. Shevlin, S. M. Woodley, A. A. Sokol, and A. Walsh, Chem. Mater. **27**, 3844 (2015).

[7] A. J. Martinolich, J. A. Kurzman, and J. R. Neilson, J. Am. Chem. Soc. **137**, 3827 (2015).

[8] B.-R. Chen, W. Sun, D. A. Kitchaev, J. S. Mangum, V. Thampy, L. M. Garten, D. S. Ginley, B. P. Gorman, K. H. Stone, G. Ceder, M. F. Toney, and L. T. Schelhas, Nat. Comm. **9**, 2553 (2018).

[9] P. K. Todd, A. M. M. Smith, and J. R. Neilson, Inorg. Chem. **58**, 15166 (2019).

[10] P. K. Todd and J. R. Neilson, J. Am. Chem. Soc. **141**, 1191 (2019).

[11] E. G. Rognerud, C. L. Rom, P. K. Todd, N. R. Singstock, C. J. Bartel, A. M. Holder, and J. R. Neilson, Chem. Mater. **31**, 7248 (2019).

[12] P. K. Todd, A. J. Martinolich, and J. R. Neilson, Chem. Commun. (2020), doi: 10.1039/D0CC03397A.

[13] H. He, C. H. Yee, D. E. McNally, J. W. Simonson, S. Zellman, M. Klemm, P. Kamenov, G. Geschwind, A. Zebro, S. Ghose, J. Bai, E. Dooryhee, G. Kotliar, and M. C. Aronson, Proc. Natl. Acad. Sci. U.S.A. **115**, 7890 (2018).

[14] C. Franco, A. Wustrow, B. Xia, A. M. Baccarella, F. Burgos, J. Nicasio, E. Dooryhee, J. R. Neilson, and J. W. Simonson, Phys. Rev. Mater. **4**, 045404 (2020).

[15] M. G. Kanatzidis, Inorg. Chem. **56**, 3158 (2017).

[16] D. E. Bugaris and H.-C. zur Loye, Angew. Chem., Int. Ed. **51**, 3780 (2012).

[17] P. Strobel and B. Lambert-Andron, J. Solid State Chem. **75**, 90 (1988).

[18] J. Sugiyama, K. Mukai, H. Nozaki, M. Harada, M. Månsson, K. Kamazawa, D. Andreica, A. Amato, and A. D. Hillier, Phys. Rev. B **87**, 024409 (2013).

[19] K. Balamurugan, S.-H. Lee, J.-S. Kim, J.-M. Ok, Y.-J. Jo, Y.-M. Song, S.-A. Kim, E. S. Choi, M. D. Le, and J.-G. Park, Phys. Rev. B **90**, 104412 (2014).

[20] C. Yu, H. Wang, X. Guan, J. Zheng, and L. Li, J. Alloys Compd. **546**, 239 (2013).
[21] A. Boulineau, L. Croguennec, C. Delmas, and F. Weill, Dalton Trans. **41**, 1574 (2012).
[22] A. Boulineau, L. Croguennec, C. Delmas, and F. Weill, Chem. Mater. **21**, 4216 (2009).
[23] A. S. Menon, D. O. Ojwang, T. Willhammar, V. K. Peterson, K. Edström, C. P. Gomez, and W. R. Brant, ACS Appl. Mater. Interfaces **12**, 5939 (2020).
[24] K. Hoang, Phys. Rev. Appl. **3**, 024013 (2015).
[25] K. Hoang, Phys. Rev. Mater. **1**, 075404 (2017).
[26] K. Hoang, Phys. Rev. Mater. **1**, 075403 (2017).
[27] Y. Shin, H. Ding, and K. A. Persson, Chem. Mater. **28**, 2081 (2016).
[28] Y. Song, X. Zhao, C. Wang, H. Bi, J. Zhang, S. Li, M. Wang, and R. Che, J. Mater. Chem. A **5**, 11214 (2017).
[29] Y. Sakamura, J. Electrochem. Soc. **157**, E135 (2010).
[30] A. Lassin, C. Christov, L. André, and M. Azaroual, Am. J. Sci. **315**, 204 (2015).
[31] A. R. Kamali, D. J. Fray, and C. Schwandt, J. Therm. Anal. Calorim. **104**, 619 (2011).
[32] R. C. Clark and J. S. Reid, Acta Crystallogr., Sect. A **51**, 887 (1995).
[33] V. Petříček, M. Dušek, and L. Palatinus, Z. Kristallogr. **229**, 345 (2014).
[34] L. Palatinus and G. Chapuis, J. Appl. Crystallogr. **40**, 786 (2007).
[35] K. Momma and F. Izumi, J. Appl. Crystallogr. **44**, 1272 (2011).
[36] G. Kresse and J. Furthmüller, Comput. Mater. Sci. **6**, 15 (1996).
[37] G. Kresse and J. Furthmüller, Phys. Rev. B **54**, 11169 (1996).
[38] G. Kresse and D. Joubert, Phys. Rev. B **59**, 1758 (1999).
[39] J. P. Perdew, K. Burke, and M. Ernzerhof, Phys. Rev. Lett. **77**, 3865 (1996).
[40] A. Jain, S. P. Ong, G. Hautier, W. Chen, W. D. Richards, S. Dacek, S. Cholia, D. Gunter, D. Skinner, G. Ceder, and K. A. Persson, APL Mater. **1**, 011002 (2013).
[41] R. Xiao, H. Li, and L. Chen, Chem. Mater. **24**, 4242 (2012).
[42] A. Van der Ven, M. K. Aydinol, G. Ceder, G. Kresse, and J. Hafner, Phys. Rev. B **58**, 2975 (1998).
[43] M. G. Brik and A. M. Srivastava, J. Lumin. **133**, 69 (2013).
[44] A. M. Srivastava and M. G. Brik, Opt. Mater. **35**, 1544 (2013).
[45] J. C. Umana, A. M. Baccarella, L. Steinke, A. Geritano, Y. Janssen, M. C. Aronson, and J. W. Simonson, Phys. Rev. B **100**, 104425 (2019).
[46] S. Tamilarasan, S. Laha, S. Natarajan, and J. Gopalakrishnan, J. Mater. Chem. C **3**, 4794 (2015).
[47] S. P. Ong, W. D. Richards, A. Jain, G. Hautier, M. Kocher, S. Cholia, D. Gunter, V. L. Chevrier, K. A. Persson, and G. Ceder, Comput. Mater. Sci. **68**, 314 (2013).
[48] K. Lejaeghere, V. Van Speybroeck, G. Van Oost, and S. Cottenier, Crit. Rev. Solid State Mater. Sci. **39**, 14 (2014).
[49] S. Lee, S. Choi, J. Kim, H. Sim, C. Won, S. Lee, S. A. Kim, N. Hur, and J.-G. Park, J. Phys: Condens. Matter **24**, 456004 (2012).
[50] Y. Shin and K. A. Persson, ACS Appl. Mater. Interfaces **8**, 25595 (2016).
[51] J. R. Croy, J. S. Park, F. Dogan, C. S. Johnson, B. Key, and M. Balasubramanian, Chem. Mater. **26**, 7091 (2014).
[52] D. Ye, G. Zeng, K. Nogita, K. Ozawa, M. Hankel, D. J. Searles, and L. Wang, Adv. Func. Mater. **25**, 7488 (2015).
[53] Y. Sun, H. Cong, L. Zan, and Y. Zhang, ACS Appl. Mater. Interfaces **9**, 38545 (2017).